In vivo characterization of the downfield part of ^{1}H MR spectra of human brain at 9.4T:

Magnetization exchange with water and relation to conventionally determined metabolite content

Nicole D. Fichtner [1,2,3,4,†] ,Ioannis-Angelos Giaptizakis[5,6,†], Nikolai Avdievich[5], Ralf Mekle[7], Daniel Zaldivar[5], Anke Henning[8,5], Roland Kreis[1,2]

1 Department of Radiology, Neuroradiology, and Nuclear Medicine, University of Bern, Bern, Switzerland;

2 Department for BioMedical Research, University of Bern, Bern, Switzerland;

3 Graduate School for Cellular and Biomedical Sciences, University of Bern, Bern, Switzerland;

4 Institute for Biomedical Engineering, UZH and ETH Zurich, Zurich, Switzerland;

5 Max Planck Institute for Biological Cybernetics, Tübingen, Germany;

6 Graduate School of Neural and Behavioural Sciences, Tübingen, Germany;

7 Center for Stroke Research Berlin (CSB), Charité Universitätsmedizin Berlin, Berlin, Germany

8 Institute of Physics, Ernst-Moritz Arndt University Greifswald

†These authors contributed equally to this work.

Corresponding author:

Roland Kreis, Dr. sc. nat., Department for BioMedical Research/AMSM, University of Bern, Erlachstrasse 9a, CH-3012 Bern, Switzerland. E-mail: roland.kreis@insel.ch

source: https://doi.org/10.7892/boris.108911 | downloaded: 5.5.2023

Final authors' version of "Fichtner et al. Magn Reson Med. epub 2017 Oct 16. doi: 10.1002/mrm.26968"

Abstract:

Purpose: To perform exchange-rate measurements on the in vivo human brain downfield spectrum (5-10ppm) at 9.4T and to compare the variation in concentrations of the downfield resonances and of known upfield metabolites to determine potential peak labels.

Methods: Non-water suppressed metabolite cycling was used in combination with an inversion transfer technique in two brain locations in healthy volunteers to measure the exchange rates and T_1 values of exchanging peaks. Spectra were fitted with a heuristic model of a series of 13 or 14 Voigt lines, and a Bloch-McConnell model was used to fit exchange rate curves. Concentrations from non-water inverted spectra upfield and downfield were compared.

Results: Mean T_1 values ranged from 0.40 to 0.77 s and exchange rates from 0.74 to 13.8 s^{-1}. There were no significant correlations between downfield and upfield concentrations, except for NAA, with a correlation coefficient of 0.63 and $p<0.01$.

Conclusions: Using ultra-high field allowed improved separation of peaks in the 8.2-8.5ppm amide proton region, and the exchange rates of multiple downfield resonances including the 5.8ppm peak, previously tentatively assigned to urea, were measured in vivo in human brain. Downfield peaks are comprised of overlapping components, and largely missing correlations between upfield and downfield resonances – though not conclusive – indicate limited contributions from metabolites present upfield to the downfield spectrum.

Key words: proton MR spectroscopy; 9.4T; human brain; metabolites; downfield; T_1 relaxation time; exchange rates;

Final authors' version of "Fichtner et al. Magn Reson Med. epub 2017 Oct 16. doi: 10.1002/mrm.26968"

Introduction

Proton magnetic resonance spectroscopy (MRS) is a non-invasive method which can detect metabolites and quantify their concentrations and other characteristics as well as any pathological changes in these parameters. Recent development and optimization of non-water suppressed spectroscopy for in vivo experiments (1,2) has expanded the range of measurable peak characteristics to include exchange rates. The use of water suppression causes exchanging peaks to be suppressed, complicating quantification. Using a non-water suppressed sequence allows not only for improved quantification, but also for exchange rate measurements using methods such as inversion transfer. In particular, several peaks on the downfield side of water (typically between 5.0 – 10.0 ppm) have protons which exchange with water. In contrast, no peaks on the upfield (right) side of the water peak have direct chemical exchange with water, although there is some evidence of magnetization transfer effects (3). As yet, the downfield peaks remain mostly unlabeled, although previous studies on in vivo human downfield brain spectroscopy have investigated exchange rates or relaxation rates at a range of field strengths (2,4-6).

Exchange rates are of interest not only for optimization of spectroscopy experiments and sequence parameters, but also for pathology where concentrations may vary with the degree of disease severity or metabolic activity, or where exchange rates may vary with changes in pH. Chemical Exchange Saturation Transfer (CEST) experiments in particular take advantage of exchange to measure the enhanced signal from exchanging species (7), and have thus far been able to investigate tumour severity and treatment, for example, using amide proton transfer as well as dynamic glucose-enhanced experiments (8,9). CEST can measure exchange from a range of species with varying exchange rates, and mostly investigates species downfield of water; increased knowledge of the downfield resonances is therefore also of interest for the CEST community.

Although suggestions of labels for several downfield resonances have been made (4,10), most remain unlabeled. Additional characterization of downfield peaks and comparison to upfield concentrations in different brain locations may aid in determining peak labels. Furthermore, ultra-high field strengths may aid due to the advantage of improved peak separation and increased signal to noise ratio (SNR), leading to acquisition of smaller, more homogeneous voxels within reasonable measurement times. However, as field strength is increased, the shorter T_2 values of the peaks (11,12) require sequences with short echo time (TE) in order to minimize signal loss. In addition, at 9.4 T, even more so than at 7 T, B_1 radiofrequency (RF) field inhomogeneity and power drop-off within the brain may render it difficult to

Final authors' version of "Fichtner et al. Magn Reson Med. epub 2017 Oct 16. doi: 10.1002/mrm.26968"

achieve sufficient transmit power in the areas of interest (13). Therefore for these experiments, performed at 9.4 T for improved peak separation, a home-built coil with appropriate power distribution and phase increment (14), and a short-TE sequence, STimulated Echo Acquisition Mode (STEAM) (15) were used for enhanced acquisition. In order to perform exchange rate measurements, the metabolite cycling (MC) (1) non-water suppressed sequence was used in combination with inversion transfer to investigate in vivo brain metabolites. Furthermore, both upfield and downfield data were acquired in two different brain locations to compare known metabolite concentrations to downfield peak concentrations.

Methods

Subjects

Eleven healthy volunteers (mean age: 28 ± 3 years, 8 males and 3 females) were scanned for the occipital region study, and another eleven healthy volunteers (mean age: 27 ± 5 years, 7 males and 4 females) were scanned for the left parietal white matter (WM) study. Written informed consent was given by all subjects before the examination, and the study had been approved by the local ethics board. Spectra from two volunteers from the WM group were not included in analysis due to excessive motion artifacts in one or more of the data sets.

Hardware setup and RF coil

All measurements were carried out on a Siemens 9.4 T whole-body MRI scanner (Erlangen, Germany) equipped with a SC72 gradient system with a maximal nominal amplitude of 40 mT/m and a maximal slew rate of 200 T/m/s. A home-built proton coil with eight transmit and sixteen receive channels was used (16). Available peak power from the amplifiers was 8 kW with 50% line loss. The coil was tuned and matched for each volunteer individually before the beginning of the experiment using a homebuilt tuning and matching box (17) and a portable probe tuning device (Morris Instruments Inc., Canada), ensuring minimal reflected power.

For this work, we used a 16-channel phased array consisting of 8 overlapped transceiver loops (10 cm square loops) placed on an elliptical holder (clearance 23 cm height x 20 cm width) parallel to its surface, i.e. “horizontal” loops, and 8 receive-only loops each located at the center of the “horizontal” loops perpendicularly to the surface of the holder, i.e. “vertical” loops (16). To increase the amount of RF

Final authors’ version of “Fichtner et al. Magn Reson Med. epub 2017 Oct 16. doi: 10.1002/mrm.26968”

power delivered to local surface coils we used 2-way and 3-way splitters with 90° phase shift between the channels. More details on the array design are published elsewhere (16).

Data Acquisition

High-resolution images from 2D FLASH scans (in-plane resolution: 0.7x0.7 mm^2, slice thickness: 3.5 mm, 25 slices) were acquired in axial, sagittal and coronal orientations to facilitate the placement of spectroscopic voxels. For the study on a region of interest (ROI) in left parietal white matter (subsequently referred to as the WM ROI) a 4.0x2.0x1.5 cm^3 voxel was placed in the left cerebral white matter (average composition (14): WM: 78.6%, GM: 19.3%, cerebrospinal fluid (CSF): 2.0%). For the study on a slightly more grey matter-enriched area (subsequently referred to as the occipital ROI), a 2.0x2.0x3.0 cm^3 voxel was selected in a mixed gray and white matter area in the occipital lobe (average composition (18)): WM: 54.8%, GM: 41.5%, CSF: 3.6%). Both voxel positions are shown in **Figure 1:** . In particular, for the voxel located in the occipital lobe, only the three bottom coil elements were utilized, while in the case of the left cerebral white matter, the two left lateral coil elements were driven. For both voxel placements, first and second order B_0 shimming was performed using FASTESTMAP (19) and voxel-based power calibration was executed (20).

Localized single voxel downfield (NEX: 96) and upfield spectra (NEX: 64) were acquired from each volunteer for both brain regions using MC STEAM (TE/TM/TR: 10/50/5000 ms). In particular, a STEAM sequence was incorporated with an asymmetric adiabatic inversion pulse [1] during the mixing time optimized for MC at 9.4 T (18). For the selection of the three orthogonal slices, a hamming-filtered 90 degree sinc pulse with a bandwidth of ~8 kHz was used. The asymmetric adiabatic inversion pulse had a duration T_p: 22.4 ms and it was constructed of the first half of a sech pulse ($HS_{1/2}$, R = 31.415) for 0.9 T_p and the second half of a tanh/tan pulse (R=100) for 0.1 T_p. The detailed nomenclature and the pulse parameters are described in the study of Hwang et al. [1]. In this study, the asymmetric inversion pulse was applied with a minimum B_1^+: 22μT and Tx frequency: ± 350 Hz. Moreover, the frequency sweep range of the frequency modulation extended from -22.7 kHz to 0.24 kHz (18).

For the measurement of magnetization transfer between water and protons from downfield resonances, the MC STEAM localization scheme was preceded by a frequency selective pulse of duration 40 ms for the inversion of the water resonance (Hamming-filtered sinc pulse, bandwidth: 100 Hz) with varying inversion delay times (41, 96, 171, 321, 671, 1321, 3021 ms, NEX: 96). Data were acquired with 4096 time-points and an 8 kHz spectral width. A phase cycling scheme of 16 steps was implemented. In

Final authors' version of "Fichtner et al. Magn Reson Med. epub 2017 Oct 16. doi: 10.1002/mrm.26968"

order to center the voxel at the correct frequency, the transmit reference frequency for the localization pulses of MC STEAM was set at 7 ppm for the acquisition of downfield spectra and at 2.3 ppm for upfield data. Neither water presaturation nor outer volume suppression (OVS) was applied. Finally, to avoid any influence of MC pulses on absolute quantification, water reference signals (NEX: 16) were measured without MC or WS. The total exam time for each subject was approximately 90 min.

MRS Data Analysis

All data were saved in raw format and exported and reconstructed in Matlab (MATLAB and Statistics Toolbox Release 2014b, The MathWorks, Inc., Natick, Massachusetts, United States). Data were processed using home-written software for frequency alignment in the time domain based on the non-water suppressed spectra (18,21), averaging, eddy current correction (22), and coil combination using singular value decomposition based on the MC water data (23). Scaling of even- vs. odd-numbered acquisitions with a scaling factor F_s was performed to account for the asymmetric effect of the metabolite cycling pulse applied alternately on either side of the water peak (1). Zeroth- and first-order phasing were performed manually on the individuals' spectra using jMRUI (24). The spectra from the different inversion times were aligned between volunteers, and the complete data sets from the best nine subjects from each of WM and GM were averaged to create model spectra. Non-water suppressed water data were processed using the same methods.

Both water and downfield metabolite spectra were fitted similarly to previous work (4) using the Fitting Tool for Arrays of Interrelated Datasets (FiTAID (25)) by developing a model using the averaged data sets. Prior knowledge was defined with thirteen peaks for supra-ventricular and fourteen peaks for occipital lobe in the 5.5-9 ppm region (see Figure 1). The peak from NAA at 7.82 ppm was defined as a binary pattern as modeled in VeSPA (26), while homocarnosine (hCs) was defined at two locations, 7.05 and 8.02 ppm, as was previously found to be reasonable (4,27). Other lines used in the model were based on visual appearance of the peaks, and also included several broad lines to account for the baseline of the spectrum, a line to fit the residual water, and numerical spectral patterns (25) as modeled in VeSPA to account for the upfield spectra and baseline. Fitting errors for the concentrations were determined as Cramer–Rao Lower Bounds (CRLB) (28). Peak concentrations from FiTAID were scaled by the appropriate average water scaling factor: 75% (41056 mM) for GM (18) and 69% (38348 mM) for WM (14) based on previous work using the same voxel placement. In order to obtain these average water scaling factors in the prior publication, average GM, WM, and CSF percentages for each examined voxel were calculated using a homebuilt MATLAB script which utilized segmentation

Final authors' version of "Fichtner et al. Magn Reson Med. epub 2017 Oct 16. doi: 10.1002/mrm.26968"

algorithms within SPM8 (Institute of Neurology, University College London) and 3D MPRAGE images (voxel size: 1x1x1 mm3) that had been acquired for each volunteer at 3 T. In particular, the 9.4 T MPRAGE image from each volunteer was registered on the corresponding 3 T image assuming a rigid body transformation, and the calculated transformation matrix was then used to transform the spectroscopy voxel to the 3 T MPRAGE image. The specific values for the water scaling factor (W_{SF}) were calculated using the following:

$$W_{SF} = 55126\ \text{mM} \cdot \frac{(f_{GM} \cdot a_{GM} + f_{WM} \cdot a_{WM} + f_{CSF} \cdot a_{CSF})}{1 - f_{CSF}}$$

where 55126 mM is the concentration of pure water at body temperature, f_{GM}, f_{WM} and f_{CSF} correspond to the GM, WM and CSF volume percentages respectively, and the relative densities of NMR-visible water ($a_{GM} = 0.78, a_{WM} = 0.65, a_{CSF} = 0.97$) were taken from (29). Differences in downfield concentrations between occipital and WM ROIs were compared using the Wilcoxon rank-sum test.

Upfield spectra were fitted using LCModel (30), with methods similar to previously published work (18). In particular, a basis set consisting of 19 metabolites (alanine, aspartate, creatine, GABA, glucose, glutathione, glutamate, glutamine, GPC, glycine, lactate, myo-inositol, NAA, NAAG, phosphocholine, phosphocreatine, phosphorylethanolamine, scyllo-inositol, taurine) was simulated with PyGAMMA (31) based on experimentally measured chemical shifts and J-coupling values (32-34). The MC STEAM basis set was simulated using a STEAM sequence with ideal pulses. Measured macromolecular templates for both brain regions were included in the model (14). In addition, the hidden parameter of LCModel DKNTMN, which controls the baseline rigidity, was set to 0.6. A minor lipid contamination in a few subjects due to the absence of OVS was handled by omitting a section of the spectrum from 1.1-1.8 ppm from the χ^2 fit range (using the PPMGAP parameter)[2] in order to prevent a potential artifactual influence on the estimation of the macromolecular content. For the upfield spectrum, absolute metabolite concentrations in mM ($[\text{Met}]_{\text{mM}}$) without correction for relaxation were calculated using LCModel water normalized concentrations ($[\text{Met}]_{\text{Nwater}}$) through the following equation:

$$[\text{Met}]_{\text{mM}} = [\text{Met}]_{\text{Nwater}} \cdot W_{SF} \cdot \frac{2}{1 + F_s}$$

where W_{SF} is the mean water content as described earlier, and the factor $\frac{2}{1+F_s}$ was introduced to correct for the multiplication of even numbered acquisitions with F_s (1). Due to likely effects of motion between the upfield scans (acquired first) and the non-MC, non-water suppressed water scans used for

Final authors' version of "Fichtner et al. Magn Reson Med. epub 2017 Oct 16. doi: 10.1002/mrm.26968"

scaling (acquired last), the upfield GM concentrations showed large inter-subject variations. In order to remove the effects of the variable water reference on the occipital ROI upfield data, the upfield occipital ROI metabolite concentrations were rescaled based on the total creatine (tCr) peak.[1]

For WM ROIs and for downfield occipital ROIs, the water variances were smaller and therefore the concentrations were left relative to water. Spearman correlation coefficients and statistical significance were calculated between several downfield peak areas and upfield metabolite concentrations; Spearman testing was used due to the small sample size (N = 20). The 6.8, 7.0, 7.3, 8.2, 8.3, and 8.5 ppm peaks were compared to glutathione, GABA, glutamine, glutamate, or total glutamine/glutamate (Glx), which were several of the suggested assignments for those downfield peaks. Correlation coefficients were also calculated between the overall upfield macromolecule concentration and the 6.8, 7.0, and 7.3 ppm peaks downfield. For the WM ROI, where concentrations were not rescaled relative to tCr, comparisons were also made between the downfield peak at 6.8 ppm and tCr from the upfield spectra.

Magnetization Exchange Model

Exchange between the longitudinal magnetization of inverted water and the downfield metabolites was modeled using the Bloch-McConnell equations for a two-pool system (35). The model started with an initial magnetization of zero for both pools, considered as saturation recovery after the STEAM localization sequence. The second step consisted of the subsequent inversion pulse and recovery, with the corresponding initial conditions after the saturation recovery phase, as in previous published downfield work (2). The third step included numerical simulations using the Bloch-McConnell equations, ideal pulses, and phase dispersion into four equal components to account for exchange and recovery during the STEAM sequence itself. The MC pulse was simplified as an ideal non-adiabatic RF pulse with the assumption that only the metabolites were affected. The water T_1, equilibrium magnetization, and inversion pulse efficiency, which were used as constants in the fitting of the exchange curves of the metabolite peaks, were determined using an inversion recovery model in FiTAID (25), using three components for water: brain water, cerebrospinal fluid water, and myelin water, the latter two of which had upper limits of, respectively, 10% and 5% for GM and 5% and 10% for WM. The inversion pulse efficiency was found to be lower than expected (yielding an effective average flip angle of 117° for the WM ROI, and 126° for the occipital ROI), which made its inclusion in the model necessary to account for reduced inversion and therefore less exchange than expected for an ideal 180° pulse. Six peaks were modeled for exchange in WM: 5.8 ppm, 6.8 ppm, 8.2 ppm, 8.3 ppm, 8.5 ppm, and a combined NAA and broader underlying component (taken separately, neither component yielded a reasonable exchange

Final authors' version of "Fichtner et al. Magn Reson Med. epub 2017 Oct 16. doi: 10.1002/mrm.26968"

curve). An additional peak at 7.3 ppm was fitted for the occipital ROI. The exchange curves yielded T_1 and exchange rates for the various metabolite peaks fitted. For occipital lobe, the individual data sets for 7.3 ppm were not fitted due to larger errors in the individual points; for this case, only the average data set was fitted. Exchange rates and T_1 values were compared between occipital and WM ROIs using the Wilcoxon rank-sum test.

Results

Averaged results for non-water inverted, non-water suppressed spectra for both WM and occipital ROIs are shown in **Figure 2**. Several peaks show exchange over the different inversion times, as they decrease in amplitude before recovering again, with the 5.8 ppm peak and the 8.2-8.5 ppm peaks in particular showing fast exchange, decreasing to close to 0 by 300 ms. Exchanging peaks fitted using the exchange model are highlighted by red arrows for fast exchange, and blue for apparent slower exchange, which was in some cases not quantifiable. An individual data set from one volunteer for the occipital ROI, including fit and residuals, are shown in **Figure 3** as a sample of data quality (an individual data set from one volunteer for the WM ROI can be seen in Supporting Figure S1 found online). Appropriateness of the model can be determined from the residuals from both the model shown in Figure 1, and the individual data set. Upfield spectra from the same volunteers as in Figure 3 are shown in **Figure 4**, along with the corresponding LCModel fits, baselines, and residuals.

Mean downfield concentrations found from the non-water inverted spectra for the peaks of interest are shown in **Table 1**, with errors given as standard deviations over the cohort. Specifically, homocarnosine, the 6.0 ppm peak, the 7.3 ppm peak, the 8.3 ppm peak, and NAA show significant differences between WM and occipital lobe with $p < 0.05$. For comparisons between upfield and downfield peak areas, NAA was found to have a Spearman correlation coefficient of 0.63 and $p < 0.01$; the corresponding NAA scatter plot can be seen in **Figure 5**. No other correlations with $p < 0.1$ were found for any of the combinations of the downfield peaks to upfield metabolite concentrations described in the methods; corresponding scatter plots for these combinations are shown in Supporting Figure S2 found online.

Boxplots for T_1 values and exchange rates are shown in **Figure 6** and **Figure 7**, respectively. **Table 2** shows mean values for T_1 and exchange rates. Mean metabolite T_1 values ranged from 0.22 s for the 8.3 ppm peak in the occipital ROI up to 0.77 s for the 5.8 ppm peak in WM. Fitted exchange curves for the exchanging peaks are shown for the average WM and occipital ROI series in **Figure 8**. Exchange rates were within a range of 0.74 s^{-1} for the combined NAA peak in the occipital ROI to 13.8 s^{-1} for the 8.3 ppm

Final authors' version of "Fichtner et al. Magn Reson Med. epub 2017 Oct 16. doi: 10.1002/mrm.26968"

peak in the occipital ROI. The 7.3 ppm peak for the average occipital ROI series yielded a T_1 of 0.42 s and an exchange rate of 1.9 s^{-1}. Between WM and occipital ROIs, the only significant differences found ($p < 0.05$) were for T_1 values for the 8.2 and 8.3 ppm peaks, as highlighted in Figure 6.

Discussion

The non-water suppressed spectra acquired in this study provided improved spectral resolution and higher exchanging peak intensity compared to lower field strength (2) or water-suppressed experiments (4), yielding in particular further separable peaks in the 8.2-8.5 ppm region and additional exchanging peaks closer to water. The inversion transfer experiments performed allowed the evaluation of thirteen or fourteen peaks for WM and occipital ROIs, respectively, for extraction of concentrations and, for several of the peaks, exchange rates and T_1 relaxation values. This study also included upfield data in both WM and occipital ROIs for additional peak concentration comparisons in order to determine any correlations between known upfield metabolite concentrations and the unknown downfield resonances.

Concentrations

The concentrations of the downfield metabolites from the two ROIs were significantly ($p < 0.05$) different for a few peaks only: homocarnosine, the 6.0, 7.3, and 8.3 ppm peaks, and NAA; they were not significantly different for the remainder. Standard deviations for most of the peaks were relatively small, indicating good agreement across subjects. The 5.8 ppm peak, being closer to water and therefore more prone to any artifacts related to imperfect water cancelation, was slightly more difficult to fit and hence has a somewhat larger standard deviation. The 7.3 ppm peak may be different due to the additional modeling of the 7.4 ppm for the occipital ROI. The concentration of the narrow NAA doublet in the occipital ROI was 10.5 ± 1.2 mM and in the WM ROI it had a value of 8.4 ± 1.5 mM, which was found to be significantly different ($p < 0.05$). Both of these values are in agreement with previously published work on NAA concentrations (36). Homocarnosine was found to be significantly higher in the occipital ROI at 1.02 ± 0.49 mM than in WM at 0.35 ± 0.21 mM. This difference may be due to the fitting model and procedure, since the concentrations are low, but may also be due to differences between voxel locations. However, previous literature is in disagreement over whether or not a difference is expected (37). If so, the WM ROI would be expected to have a higher concentration than occipital ROI, contrary to what was seen in the present study. Other resonances have concentrations that are lower than those found at 7 T (4), possibly related to the presence of broad underlying components which were additionally included in the fitting model at 9.4 T, for example in the range of 6.8-7.3 ppm, where the

Final authors' version of "Fichtner et al. Magn Reson Med. epub 2017 Oct 16. doi: 10.1002/mrm.26968"

concentrations at 9.4 T are lower than at 7 T. Differences between the 9.4 T and 7 T experiments are also expected due to the use of water suppression at 7 T, where exchanging peaks would be reduced. Concentrations of the 6.0 and 6.1 ppm peak are higher at 9.4 T than at 7 T, which is likely due to the presence of slow exchange. Similarly, concentrations of resonances in the 8.2-8.5 ppm region could not be compared, due to fast exchange and the use of water suppression at 7 T.

Correlations between downfield peaks and upfield representations of metabolites were of particular interest for these experiments, in order to investigate potential labels for peaks as previously indicated in the literature (4,10). As expected, downfield NAA positively correlates with upfield NAA concentrations, with a Spearman correlation coefficient of $r = 0.63$ ($p < 0.01$). However, none of the other downfield peaks significantly correlates with upfield metabolite concentrations. Of course, significant correlations can only be expected if there is sufficient true variation in metabolite content within the cohort at a limited random variance level. For all the tested candidate metabolites the cohort variance in upfield concentration was larger than that for upfield NAA and one could expect this variance to be reflected downfield, but no significant covariance was detected. Thus, while these and other upfield metabolites may certainly still be present as small components of the different downfield peaks, they do not appear to dominate any of the downfield peaks.

Exchange fitting

Although up to fourteen peaks were fitted in the spectra, several did not evidence exchange in these experiments, or had such slow exchange that its quantification was not possible. Exchange rates and T_1 values were obtainable only through the Bloch-McConnell model used for fitting the exchanging peaks, and are therefore only presented for the exchange-modeled peaks. It should be noted that many of the resonances downfield are quite broad, indicating a potential for several underlying components; even exchanging peaks may be composed of more than one component, with potentially different exchange rates for different components. However, the required simplicity of the model led to fitting the visible resonances with single peaks, with the T_1 and exchange rates therefore corresponding to averages over the components. It can also be seen that the occipital ROI and WM ROI provide very similar exchange rates and T_1 times for the fitted peaks, as demonstrated in Figures 6 and 7, with only two significant T_1 differences between the two voxels, for the 8.2 and 8.3 ppm peaks. Similar values are expected not only because of the fairly high percentage of white matter in the occipital ROI, but also due to the equal proportions of metabolites and macromolecular baseline for WM and occipital ROIs upfield (38), therefore supporting the results found in this study.

Final authors' version of "Fichtner et al. Magn Reson Med. epub 2017 Oct 16. doi: 10.1002/mrm.26968"

Of particular interest are the peaks that were not fitted at 3 T (2), such as the 5.8 ppm peak, or the peaks which have improved separation, such as in the amide region from 8.2-8.5 ppm. The 5.8 ppm peak, which was previously suggested to originate from urea (4), has a mean exchange rate of 7.4 s^{-1} from the combined occipital ROI and WM ROI experiments; a low exchange rate on this order is expected as this peak remains visible in experiments which use water suppression (4,39). The amide region has a range of exchange rates, from a mean of 3.7 s^{-1} for the 8.5 ppm peak, which is significantly slower than the 8.9 s^{-1} found at 3 T, to 9.9 and 13.6 s^{-1}, for the 8.2 and 8.3 ppm peaks, respectively, which are higher rates than the 7.5 s^{-1} found for the broader 8.2 ppm peak fitted at 3 T (2). However, due to differences of timing and localization between the current study and the 3 T inversion transfer experiments (2), the limits of exchange that can be measured are also different. In this case, the measured amide peaks may be composed of slightly different exchanging amides, and the model used for fitting may have also captured different peaks than before. Despite the minor differences between the 3 T and 9.4 T experiments, the exchange rates found in the current study are similarly in line with the lower end of what has been reported previously for the amide region using water exchange-filtered (WEX) experiments (40).

There is also limited exchange for the three peaks in the 6.8-7.3 ppm region, although at 3 T there appeared to be greater exchange visible. These differences may be explained by the addition of a broader peak in the 9.4 T model, which would account for any subtler changes in the broader peaks that may be due to macromolecular exchange, or other slow exchange from overlapping peaks. The combined NAA and its shoulder provided an average exchange rate of 0.8 s^{-1}, which is similar to what was found for the broader NAA peak that was modeled at 3 T; individually, neither the NAA doublet nor the broader shoulder provided meaningful exchange curves and were thus exchange-modeled together. It is possible that the fitting model had not been able to properly separate out the exchanging component.

Downfield T_1 relaxation values, varying from 0.22 s to 0.77 s, are shorter than previously published upfield values at 7 and 9.4 T (41,42), and are on the order of macromolecular T_1 values, which suggests that macromolecular components are contributing to the peaks. The downfield T_1 values are also higher than those found downfield at 3 T for similar experiments (2), a finding that is expected, since proton T_1 relaxation times increase with field strength (12). While the T_1 relaxation times are similar to those at 7 T, only the order of magnitude should be compared, as the current study extracted exchange-independent times, and a previous 7 T study, which was a different experiment altogether, did not

Final authors' version of "Fichtner et al. Magn Reson Med. epub 2017 Oct 16. doi: 10.1002/mrm.26968"

account for exchange effects (4). The 6.8 ppm peak has a mean T_1 of 0.41 s, which is similar to that found for the 6.8 ppm resonance at 7 T, and again on the order of the T_1's for macromolecules. The combined NAA peak here has a much lower T_1 than that found for NAA at 7 T; however, in this case the combined NAA peak cannot give us a meaningful estimate of T_1, and was of more interest for its exchange rate. At 3 T, this peak was modeled as one peak only, due to the broader peaks at lower field strengths. T_1's for the faster exchanging peaks vary, although the low T_1 for the 8.3 ppm peak may have been partially compensated by the faster exchange rate.

Limitations

Exchange with inverted, as opposed to saturated, water magnetization, has the potential to affect the metabolite peak sizes more strongly such that for fast-exchanging species the peak may even be inverted. However, it was discovered upon fitting of the water inversion curves after all measurements had been completed that despite B_1 optimization, the effective flip angle for the water inversion pulse had not reached higher than 131°. Further investigation into the potential cause for the low inversion efficiency led to the suspicion that radiation damping (43) may have played a role in reducing the maximum signal achievable after applying the non-spatially selective inversion pulse. In addition, the long duration of the pulse (40 ms) may have allowed T_2 relaxation effects to reduce the signal during the RF pulse itself, as the pulse duration is on the order of brain water T_2 at high fields (4,44). It is likely that with 100% efficiency and a shorter duration of the inversion pulse the metabolite peaks would have evidenced exchange more strongly, improving accuracy of exchange rate and T_1 calculations.

A further experimental issue found after completion of the study was that there was an unexpectedly large asymmetry for the water signal in up- vs. down-field inverted spectra in MC. The size of the effect and the fact that downfield inverted scans showed larger water amplitude than upfield inverted acquisitions indicate that the asymmetry is not exchange-related, but more likely to be an effect of experimental asymmetry including potential frequency drift after center-frequency adjustment.

The measurable exchange rates in this experiment are limited by several factors, including the echo time and the global water inversion pulse duration. The echo time for these experiments was 10 ms, limiting our ability to measure exchange rates faster than 100 s^{-1} (corresponding lifetime of <~10 ms) as any spins exchanging too fast would no longer be properly refocused for measurement. Furthermore, the long inversion pulse duration of 40 ms meant that any fast exchange of >~25 s^{-1} would be moderated even before the inversion recovery period started, reducing the ability to properly quantify it. While this

Final authors' version of "Fichtner et al. Magn Reson Med. epub 2017 Oct 16. doi: 10.1002/mrm.26968"

pulse was optimized for a small bandwidth to reach close to water, it would be clearly more efficient to have a shorter inversion pulse for those resonances further away from water. Another limiting effect on measuring the exchange rates is evolution into out-of-phase signal due to exchange during the TM period, which was relatively long at 45 ms due to the MC pulse. This evolution into out-of-phase signal is due to differing effective chemical shifts in the half echo periods before and after TM (analogous to a single T_2-trace from a 2D exchange spectroscopy (45) experiment with an acquisition delay in T_2 equal to the T_1 dwell time (i.e = TE/2 in our case)). Based on simulations, there should be some measurable effect for faster-exchanging species. However, no such signal behavior was found in the data, leading to the conclusion that any fast-exchanging species that would lead to out-of-phase components were exchanging too fast to be measured by this experiment anyway.

It was also found that for the fast-exchanging resonances, in particular at 8.2 and 8.3 ppm, the minimum of the exchange curve often occurred at the second inversion time, rendering accurate fitting of the exchange curve difficult due to the lack of points describing the initial decrease in the exchange curve. In those cases, the recovery component of the curve had more weighting and the $M_{z,eq}$ could compensate for T_1 and k more than for the slower exchange curves. The 41 ms inversion time was already the minimum achievable on the system; however, additional points before 96 ms would have helped for the faster-exchanging resonances. Unfortunately due to restrictions on the duration of the experiment, further inversion times were not acquired.

Furthermore with regard to the missing correlations leading to labeling of downfield peaks, it should be kept in mind that the fit model for the downfield spectrum is heuristic. The specific choice of components–even though chosen as carefully as possible with Occam's razor in mind to represent the spectrum's main content—may hide some co-variance with upfield metabolites, where again some of the variance will be spurious for the smaller spectral contributions.

Conclusions

This study presents the first in-depth investigation of downfield metabolites at 9.4 T, as well as first comparisons of downfield and upfield peak concentrations. Furthermore, exchange rates and T_1 values for at least six of the twelve measured resonances downfield were calculated. Increased peak separation of the 8.2-8.5 ppm region allowed for improved characterization of the amide region and corresponding exchange rates. Moreover, for the first time it was possible to quantify the exchange rate of the 5.8 ppm peak, tentatively assigned to urea (4,39), in vivo in human brain. Correlations between downfield peaks

Final authors' version of "Fichtner et al. Magn Reson Med. epub 2017 Oct 16. doi: 10.1002/mrm.26968"

and known upfield metabolite concentrations were insignificant, except for NAA. This suggests that, while the compared metabolites might form components of these peaks, they probably do not make up a significant portion of them.

Acknowledgements

This work is supported by the Swiss National Science Foundation (SNSF #320030-156952). Part of the project (I.A Giapitzakis) was co-sponsored by the European Social Fund and national funds (NSRF 2007-2013) through the Greek State Scholarships Foundation (IKY).

Footnotes:

[1] In detail, the cohort average of total creatine was conserved from the values obtained by water-scaling, while all individual spectra were rescaled to yield identical total creatine content.

[2] It was made sure that the lipid artifact from the methylene protons was small enough such that the rest of the lipid spectrum would be too small to substantially interfere outside the excluded fitting range.

Final authors' version of "Fichtner et al. Magn Reson Med. epub 2017 Oct 16. doi: 10.1002/mrm.26968"

References

1. Dreher W, Leibfritz D. New method for the simultaneous detection of metabolites and water in localized in vivo 1H nuclear magnetic resonance spectroscopy. Magn Reson Med 2005;54:190-195.
2. MacMillan EL, Chong DGQ, Dreher W, Henning A, Boesch C, Kreis R. Magnetization exchange with water and T1 relaxation of the downfield resonances in human brain spectra at 3.0 T. Magn Reson Med 2011;65:1239-1246.
3. McLean MA, Barker GJ. Concentrations and magnetization transfer ratios of metabolites in gray and white matter. Magn Reson Med 2006 Oct 18;56(6):1365-70.
4. Fichtner ND, Henning A, Zoelch N, Boesch C, Kreis R. Elucidation of the downfield spectrum of human brain at 7T using multiple inversion recovery delays and echo times. Magn Reson Med 2016 Jul 25;doi: 10.1002/mrm.26343
5. De Graaf RA, De Feyter HM, Brown PB, Nixon TW, Rothman DL, Behar KL. Detection of Cerebral NAD+ in Humans at 7T. Magn Reson Med 2016;10.1002/mrm.26465
6. Vermathen P, Capizzano AA, Maudsley AA. Administration and (1)H MRS detection of histidine in human brain: application to in vivo pH measurement. Magn Reson Med 2000;43:665-675.
7. Ward KM, Aletras AH, Balaban RS. A New Class of Contrast Agents for MRI Based on Proton Chemical Exchange Dependent Saturation Transfer (CEST). J Magn Reson 2000;143
8. Xu X, Yadav NN, Knutsson L, Hua J, Kalyani R, Hall E, Laterra J, Blakely J, Strowd R, Pomper M, and others. Dynamic Glucose-Enhanced (DGE) MRI: Translation to Human Scanning and First Results in Glioma Patients. Tomography 2015 Dec;1(2)105-14.
9. Jones CK, Schlosser MJ, van Zijl PCM, Pomper MG, Golay X, Zhou J. Amide proton transfer imaging of human brain tumors at 3T. Magn Reson Med 2006;56
10. Henning A, Fuchs A, Boesch C, Boesiger P, Kreis R. Downfield spectra at ultrahigh field. In Proceedings of the 16th Meeting of ISMRM, Toronto, Canada, 2008. p. 777.
11. Crooks L, Arakawa M, Hoenninger J, McCarten B, Watts J, Kaufman L. Magnetic Resonance Imaging: Effects of Magnetic Field Strength. Radiology 1984;151:127-133.
12. De Graaf RA, Brown PB, McIntyre S, Nixon TW, Behar KL, Rothman DL. High magnetic field water and metabolite proton T1 and T2 relaxation in rat brain in vivo. Magn Reson Med 2006;56:386-394.
13. Vaughan JT, Garwood M, Collins CM, Liu W, DelaBarre L, Adriany G, Andersen P, Merkle H, Goebel R, Smith MB, Ugurbil K. 7T vs. 4T: RF power, homogeneity, and signal-to-noise comparison in head images. Magn Reson Med 2001;46:24-30.
14. Giapitzakis IA, Kreis R, Henning A. Characterization of the macromolecular baseline with a metabolite-cycled double-inversion recovery sequence in the human brain at 9.4T. In Proceedings of the 24th Meeting of ISMRM, Singapore, 2016. p. 0016.
15. Frahm J, Merboldt KD, Haenicke W. Localized proton spectroscopy using stimulated echoes. J Magn Reson 1987;72:502-508.
16. Avdievich N, Giapitzakis IA, Henning A. Optimization of the receive performance of a tight-fit transceiver phased array for human brain imaging at 9.4T. In Proceedings of the 25th Meeting of ISMRM, Honolulu, HI, USA, 2017. p. 4309.
17. Avdievich N, Walzog J, Steffen T, Henning A. Development of a low cost multi-channel tune and match device for transceiver arrays at high magnetic fields. In Proceedings of the 32nd Annual Scientific Meeting of ESMRMB, Edinburgh, UK, 2016. p. S445.
18. Giapitzakis IA, Shao T, Avdievich N, Mekle R, Kreis R, Henning A. Metabolite-cycled STEAM and semi-LASER localization for MR spectroscopy of the human brain at 9.4T. Magn Reson Med 2017;10.1002/mrm.26873
19. Gruetter R, Tkac I. Field mapping without reference scan using asymmetric echo-planar techniques. Magn Reson Med 2000;43:319-323.
20. Versluis MJ, Kan HE, van Buchem MA, Webb AG. Improved signal to noise in proton spectroscopy of the human calf muscle at 7 T using localized B1 calibration. Magn Reson Med 2010;63:207-211.
21. Hock A, MacMillan EL, Fuchs A, Kreis R, Boesiger P, Kollias SS, Henning A. Non-water-suppressed proton MR spectroscopy improves spectral quality in the human spinal cord. Magn Reson Med 2012;epub 2012 Jun 28. doi: 10.1002/mrm.24387
22. Klose U. In vivo proton spectroscopy in presence of eddy currents. Magn Reson Med 1990;14:26-30.
23. Bydder M, Hamilton G, Yokoo T, Sirlin CB. Optimal Phased Array Combination for Spectroscopy. Magn Reson Imag 2008;26:847-850.

Final authors' version of "Fichtner et al. Magn Reson Med. epub 2017 Oct 16. doi: 10.1002/mrm.26968"

24. Naressi A, Couturier C, Devos JM, Janssen M, Mangeat C, de Beer R, Graveron-Demilly D. Java-based graphical user interface for the MRUI quantitation package. Magn Reson Mater Phy 2001;12:141-152.
25. Chong DGQ, Kreis R, Bolliger C, Boesch C, Slotboom J. Two-dimensional linear-combination model fitting of magnetic resonance spectra to define the macromolecule baseline using FiTAID, a Fitting Tool for Arrays of Interrelated Datasets. Magn Reson Mater Phy 2011;24:147-164.
26. Soher B, Semanchuk P, Todd D, Steinberg J, Young K. VeSPA: Integrated applications for RF pulse design, spectral simulation and MRS data analysis. In Proceedings of the 19th Meeting of ISMRM, Montreal, Canada, 2011. p. 1410.
27. Rothman DL, Behar KL, Prichard JW, Petroff OA. Homocarnosine and the measurement of neuronal pH in patients with epilepsy. Magn Reson Med 1997;38:924-929.
28. Cavassila S, Deval S, Huegen C, van Ormondt D, Graveron-Demilly D. Cramer-Rao bounds: an evaluation tool for quantitation. NMR Biomed 2001;14:278-283.
29. Ernst T, Kreis R, Ross BD. Absolute quantitation of water and metabolites in the human brain. I. Compartments and water. J Magn Reson Series B 1993;102:1-8.
30. Provencher SW. Automatic quantitation of localized in vivo (1)H spectra with LCModel. NMR Biomed 2001;14:260-264.
31. Smith SA, Levante TO, Meier BH, Ernst RR. Computer simulations in magnetic resonance. An object-oriented programming approach. J Magn Reson Series A 1994;106:75-105.
32. Govind V, Young K, Maudsley AA. Corrigendum: Proton NMR chemical shifts and coupling constants for brain metabolites. Govindaraju V, Young K, Maudsley AA, NMR Biomed. 2000; 13: 129–153. NMR Biomed 2015;28
33. Govindaraju V, Young K, Maudsley AA. Proton NMR chemical shifts and coupling constants for brain metabolites. NMR Biomed 2000;13:129-153.
34. Kreis R, Bolliger CS. The need for updates of spin system parameters, illustrated for the case of gamma-aminobutyric acid. NMR Biomed 2012;epub 2012 May 14. doi: 10.1002/nbm.2810
35. McConnell HM. Reaction rates by nuclear magnetic resonance. J Chem Phys 1958;28:430-431.
36. Pouwels PJW, Frahm J. Regional metabolite concentrations in human brain as determined by quantitative localized proton MRS. Magn Reson Med 1998;39:53-60.
37. Kanazawa A, Sano RM. A method of determination of homocarnosine and its distribution in mammalian tissues. J Neurochem 1967;14:211-214.
38. Snoussi K, Gillen JS, Horska A, Puts NAJ, Pradhan S, Edden RAE, Barker PB. Comparison of brain gray and white matter macromolecule resonances at 3 and 7 Tesla. Magn Reson Med 2015;74:607-613.
39. Watanabe T, Frahm J, Michaelis T. Amide proton signals as pH indicator for in vivo MRS and MRI of the brain--Responses to hypercapnia and hypothermia. Neuroimage 2016;133:390-298.
40. van Zijl PC, Zhou J, Mori N, Payen JF, Wilson D, Mori S. Mechanism of magnetization transfer during on-resonance water saturation. A new approach to detect mobile proteins, peptides, and lipids. Magn Reson Med 2003;49:440-449.
41. Xin L, Schaller B, Mlynarik V, Lu H, Gruetter R. Proton T1 relaxation times of metabolites in human occipital white and gray matter at 7 T. Magn Reson Med 2013;69:931-936.
42. Deelchand DK, Van De Moortele PF, Adriany G, Iltis I, Andersen P, Strupp JP, Vaughan JT, Ugurbil K, Henry PG. In vivo 1H NMR spectroscopy of the human brain at 9.4 T: initial results. J Magn Reson 2010;206:74-80.
43. Krishnan VV, Murali N. Radiation damping in modern NMR experiments: Progress and challenges. Progress in Nuclear Magnetic Resonance Spectroscopy 2013;68:41-57.
44. Marjanska M, Auerbach EJ, Valabrègue R, Van de Moortele P-F, Adriany G, Garwood M. Localized 1H NMR spectroscopy in different regions of human brain in vivo at 7 T: T2 relaxation times and concentrations of cerebral metabolites. NMR Biomed 2012;25:332-339.
45. Jeener J, Meier BH, Bachmann P, Ernst RR. Investigation of exchange processes by two-dimensional NMR spectroscopy. J Chem Phys 1979;71:4546-4553.

Final authors' version of "Fichtner et al. Magn Reson Med. epub 2017 Oct 16. doi: 10.1002/mrm.26968"

Table 1: Mean downfield concentrations for both WM and occipital ROIs for the peaks of interest, presented as mean ± standard deviation over the cohort. Concentrations are obtained from the non-water-inverted spectra. Mean CRLB over the cohort are also included. It should be noted that the CRLB are only valid for a correct model, which is definitely not strictly the case in this setting, where we have composite peaks heuristically modeled as a single entity. An asterisk (*) denotes a significant difference between the occipital and the WM ROI concentrations with $p < 0.05$.

	Occipital ROI		**WM ROI**	
	Mean concentration ± SD (mM)	Mean CRLB (mM)	Mean concentration ± SD (mM)	Mean CRLB (mM)
hCs*	1.02 ± 0.39	0.141	0.35 ± 0.21	0.147
5.8 ppm	4.58 ± 1.12	0.138	4.02 ± 1.89	0.357
6.0 ppm*	1.25 ± 0.73	0.117	0.62 ± 0.36	0.238
6.1 ppm	1.21 ± 0.74	0.124	0.81 ± 0.33	0.123
6.8 ppm	2.87 ± 0.68	0.183	2.96 ± 0.82	0.294
7.0 ppm	1.96 ± 1.14	0.290	2.96 ± 0.73	0.422
7.3 ppm*	1.94 ± 0.28	0.196	2.93 ± 0.84	0.351
7.4 ppm	0.56 ± 0.21	0.124	--	--
8.2 ppm	4.16 ± 0.45	0.219	3.93 ± 0.80	0.266
8.3 ppm*	0.92 ± 0.32	0.120	0.64 ± 0.12	0.114
8.5 ppm	0.89 ± 0.32	0.106	0.78 ± 0.21	0.118
NAA*	10.52 ± 1.16	0.404	8.43 ± 1.54	0.416
NAA shoulder	4.91 ± 0.79	0.293	5.07 ± 1.15	0.333

Final authors' version of "Fichtner et al. Magn Reson Med. epub 2017 Oct 16. doi: 10.1002/mrm.26968"

Table 2: Mean exchange rates (*k*) and T_1 values for peaks fitted using the Bloch-McConnell model for occipital and WM ROIs, presented as mean ± standard deviation over the cohort. An asterisk (*) denotes a significant difference between the occipital and the WM ROI concentrations with $p < 0.05$.

	Occipital ROI exchange rate	**WM ROI exchange rate**	**Occipital ROI T_1**	**WM ROI T_1**
	Mean k ± SD (s^{-1})	Mean k ± SD (s^{-1})	Mean T_1 ± SD (s)	Mean T_1 ± SD (s)
5.8 ppm	6.76 **±** 1.59	8.00 **±** 1.63	0.65 **±** 0.16	0.77 **±** 0.11
6.8 ppm	2.34 **±** 0.44	2.42 **±** 0.69	0.40 **±** 0.03	0.41 **±** 0.04
8.2 ppm	9.32 **±** 0.91	10.6 **±** 1.50	0.46 **±** 0.12	0.69 **±** 0.18
8.3 ppm	13.8 **±** 0.79	13.4 **±** 1.77	0.22 **±** 0.09 (*)	0.41 **±** 0.14 (*)
8.5 ppm	3.31 **±** 0.06	4.05 **±** 2.12	0.71 **±** 0.14 (*)	0.76 **±** 0.20 (*)
combined NAA	0.74 **±** 0.23	0.92 **±** 0.60	0.52 **±** 0.11	0.58 **±** 0.16

Final authors' version of "Fichtner et al. Magn Reson Med. epub 2017 Oct 16. doi: 10.1002/mrm.26968"

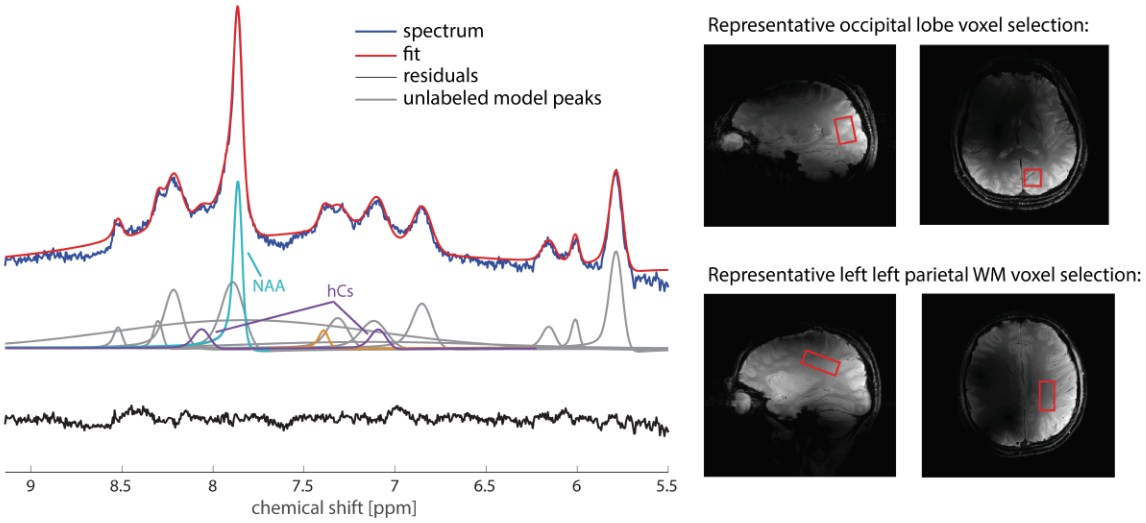

Figure 1: Averaged downfield spectrum with no water pre-inversion for the occipital ROI series, overlaid with the fitted spectrum, the model peaks (grey for unlabeled, colour for NAA and homocarnosine (hCs) with their respective labels), and with residuals shown below. Residuals indicate a decent fit for most peaks. No filtering was used. The WM ROI model is the same except for one removed peak, at 7.4 ppm, highlighted in orange. Also shown are representative locations of the voxels in the occipital lobe (above) and in the left parietal white matter region (below).

Final authors' version of "Fichtner et al. Magn Reson Med. epub 2017 Oct 16. doi: 10.1002/mrm.26968"

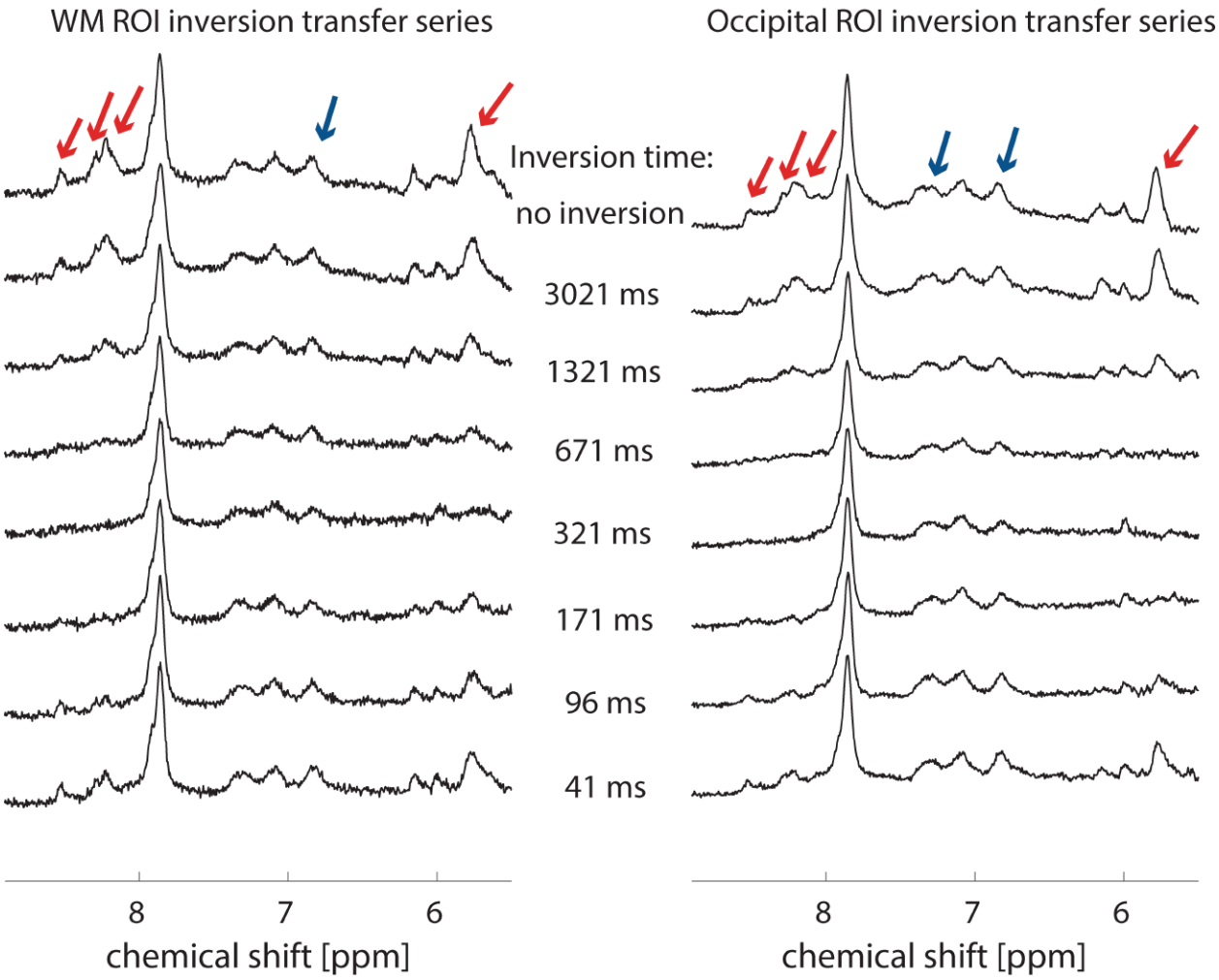

Figure 2: Averaged inversion transfer series for WM and occipital ROIs. Peaks indicated by red arrows (at 5.8, 8.2, 8.3, and 8.5 ppm) show fast exchange, leading to almost complete disappearance of the respective signals for a water inversion delay of about half a second. Peaks shown in blue also show exchange, but at a slower rate, perhaps due to the exchange being from underlying components or only part of the peak.

Final authors' version of "Fichtner et al. Magn Reson Med. epub 2017 Oct 16. doi: 10.1002/mrm.26968"

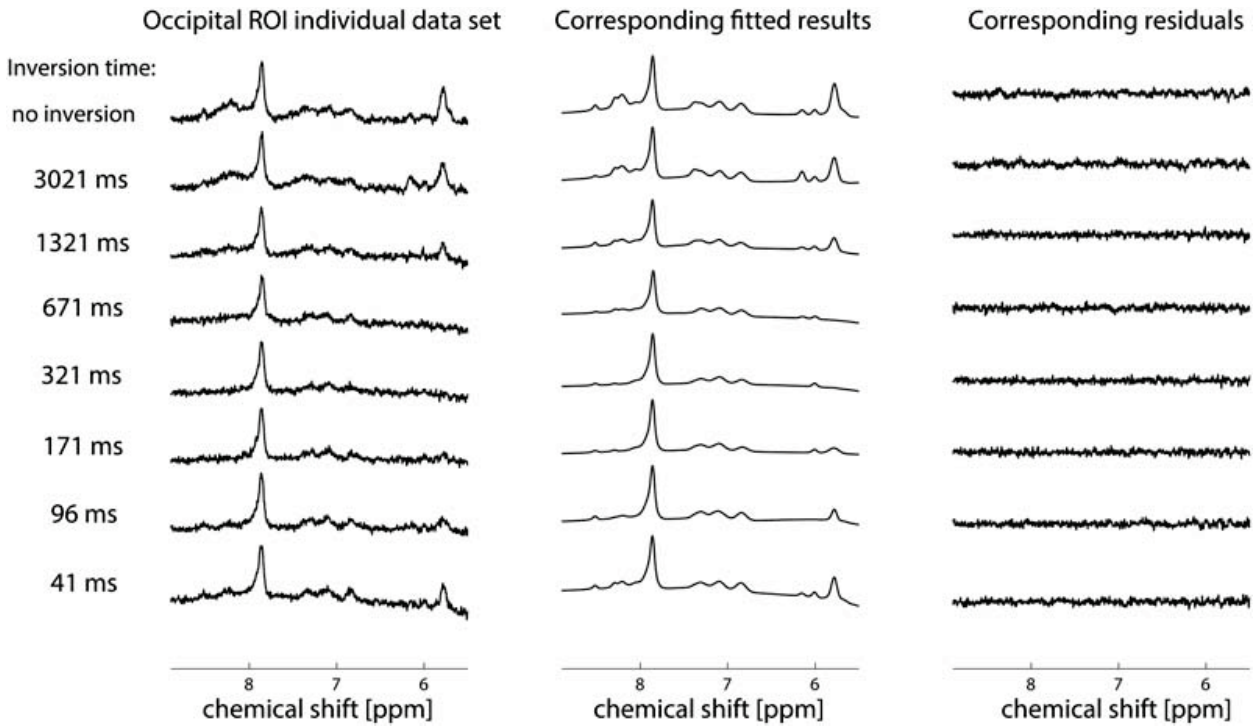

Figure 3: Representative occipital ROI inversion transfer series from an individual volunteer, along with the corresponding fitted spectra and residuals, indicating the quality of the data and the suitability of the model. For a representative inversion transfer series for the WM ROI, see Supporting Figure S1 online.

Final authors' version of "Fichtner et al. Magn Reson Med. epub 2017 Oct 16. doi: 10.1002/mrm.26968"

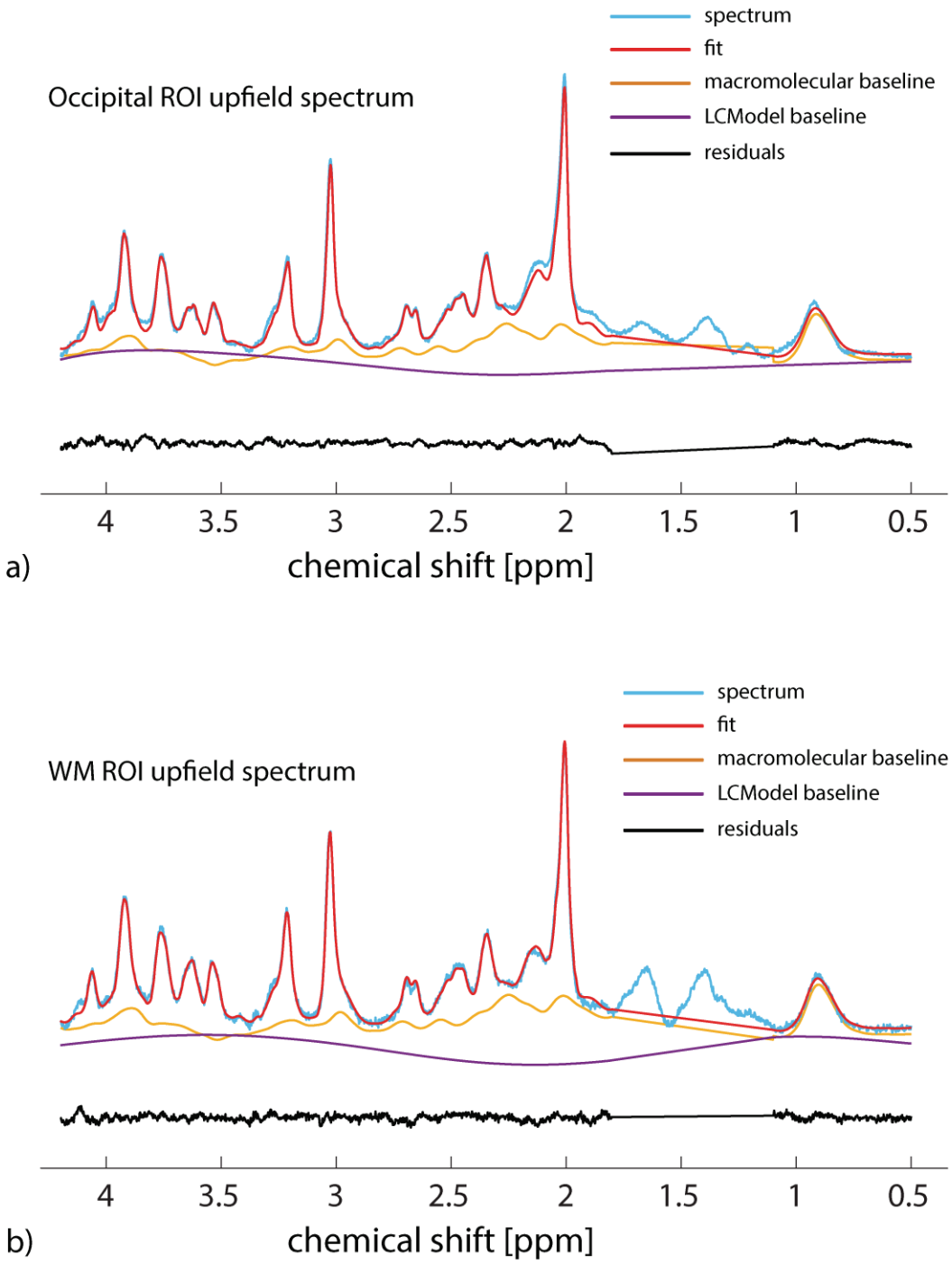

Figure 4: Representative upfield spectra along with the LCModel fits, baselines, and residuals for (a) the occipital ROI and (b) the WM ROI from the same volunteers as in Figure 3. The section between 1.1-1.8 ppm, which was not critical to the analysis, was removed from the LCModel X2 fit due to lipid artifacts as described in the methods by the PPMGAP parameter.

Final authors' version of "Fichtner et al. Magn Reson Med. epub 2017 Oct 16. doi: 10.1002/mrm.26968"

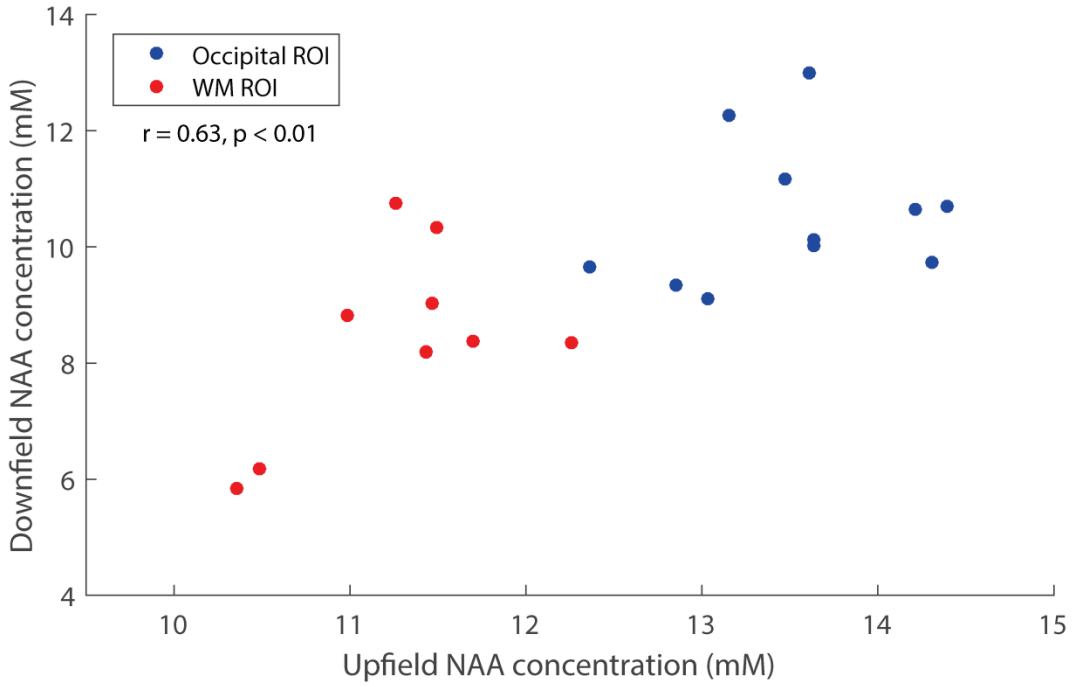

Figure 5: Scatter plot of the downfield NAA peak concentrations versus the upfield NAA concentrations, plotted with separate colours to distinguish WM ROI and occipital ROI concentrations. Scatter plots of the other correlations tested can be seen in Supporting Figure S2 online.

Final authors' version of "Fichtner et al. Magn Reson Med. epub 2017 Oct 16. doi: 10.1002/mrm.26968"

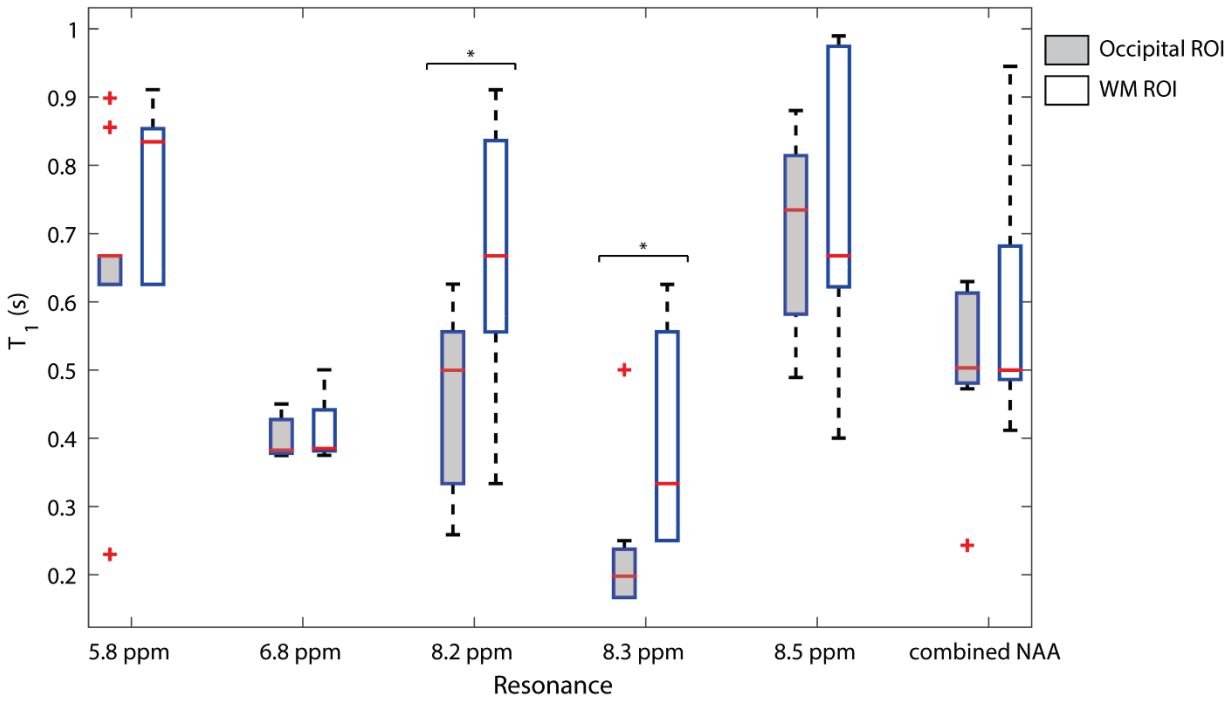

Figure 6: Boxplots indicating the range of T1 values for the different resonances fitted with the Bloch-McConnell model. The edges of the box plots are at the 25th and 75th percentiles, while the red line in between indicates the median. Whiskers extend to the extremes of the data within 1.5 times the interquartile range (if no data lies within that range, they extend to the minimum or maximum). Outliers beyond the interquartile range are denoted by a cross. Significant differences ($p < 0.05$) between WM and occipital ROIs are denoted with asterisks.

Final authors' version of "Fichtner et al. Magn Reson Med. epub 2017 Oct 16. doi: 10.1002/mrm.26968"

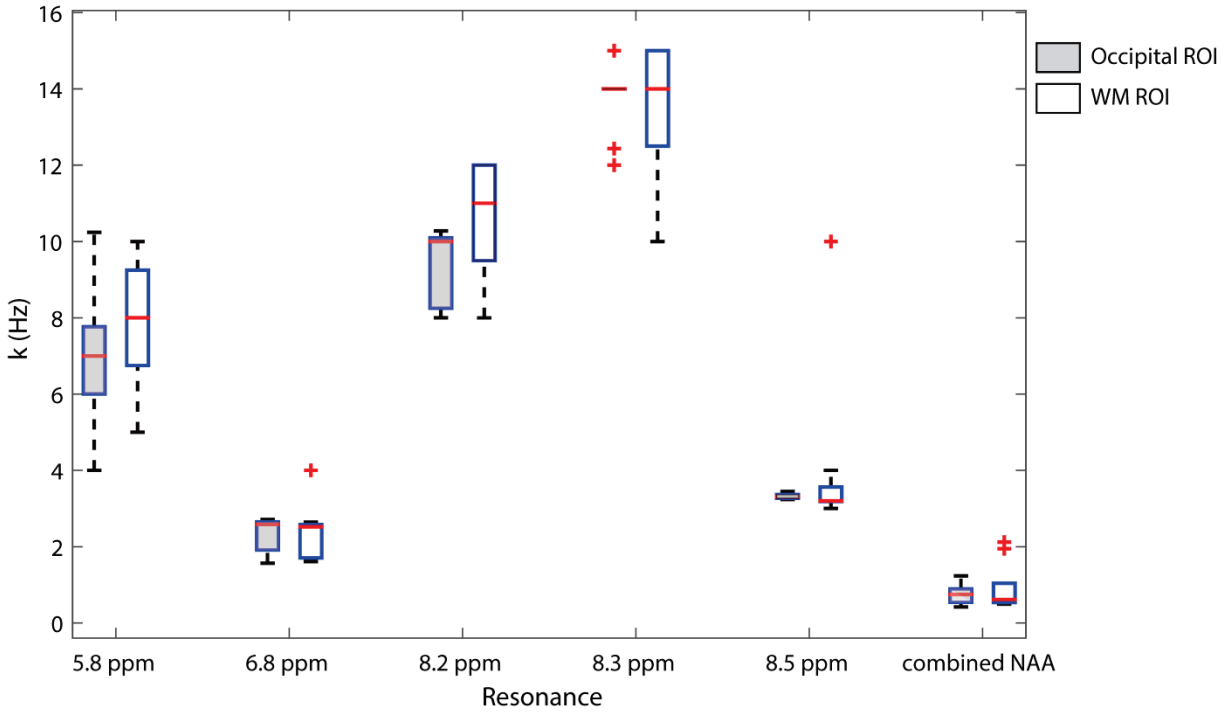

Figure 7: Boxplots indicating the range of exchange rates (k) for the different resonances fitted with the Bloch-McConnell model. The edges of the box plots are at the 25th and 75th percentiles, while the red line in between indicates the median. Whiskers extend to the extremes of the data within 1.5 times the interquartile range (if no data lies within that range, they extend to the minimum or maximum). Outliers beyond the interquartile range are denoted by a cross. No significant differences were found between white and grey matter exchange rates.

Final authors' version of "Fichtner et al. Magn Reson Med. epub 2017 Oct 16. doi: 10.1002/mrm.26968"

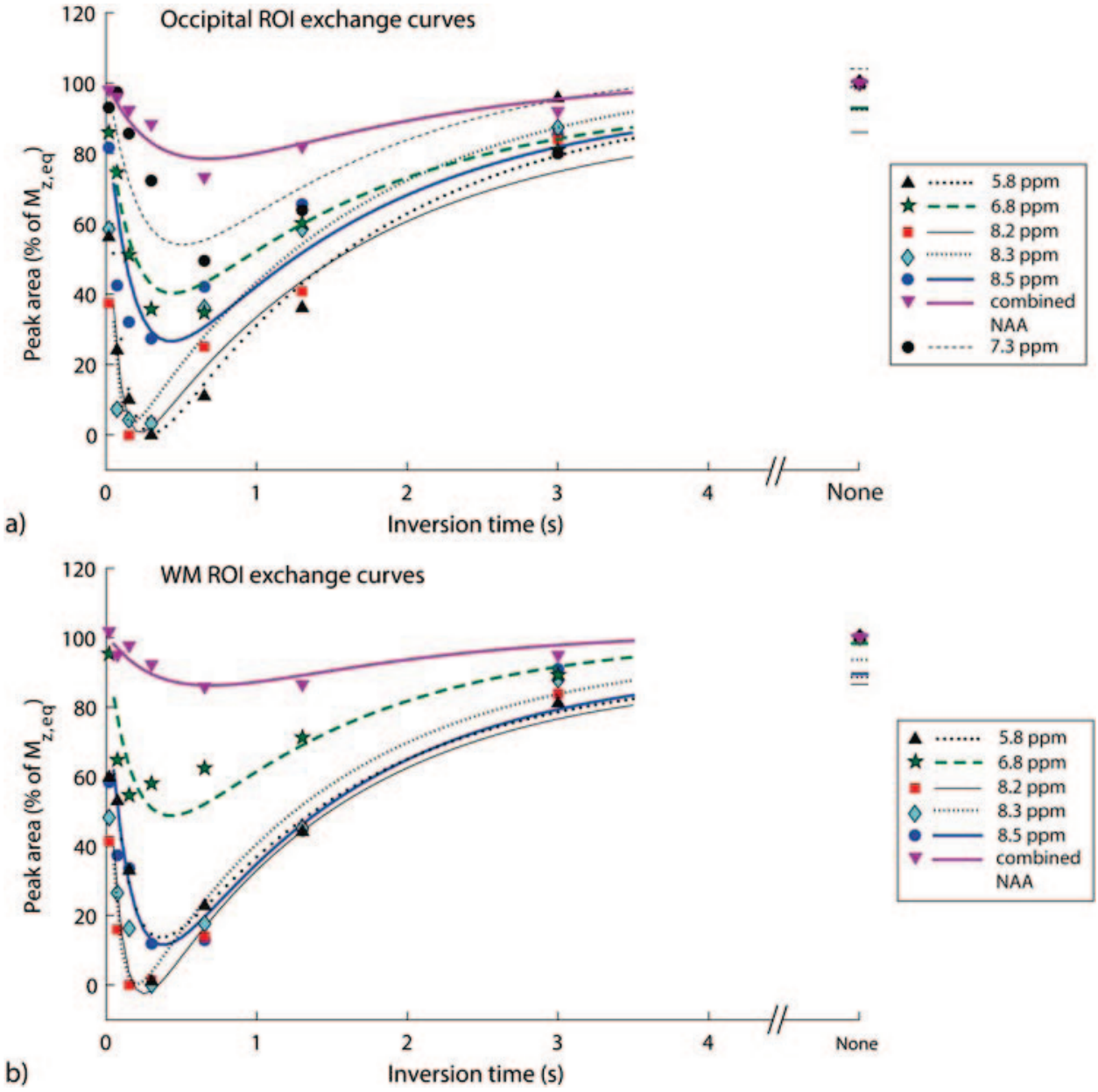

Figure 8: Exchange curves showing the peak area as a percentage of the equilibrium magnetization for (a) the occipital ROI metabolites and (b) the WM ROI metabolites that were fitted for the average over all individuals.

Final authors' version of "Fichtner et al. Magn Reson Med. epub 2017 Oct 16. doi: 10.1002/mrm.26968"

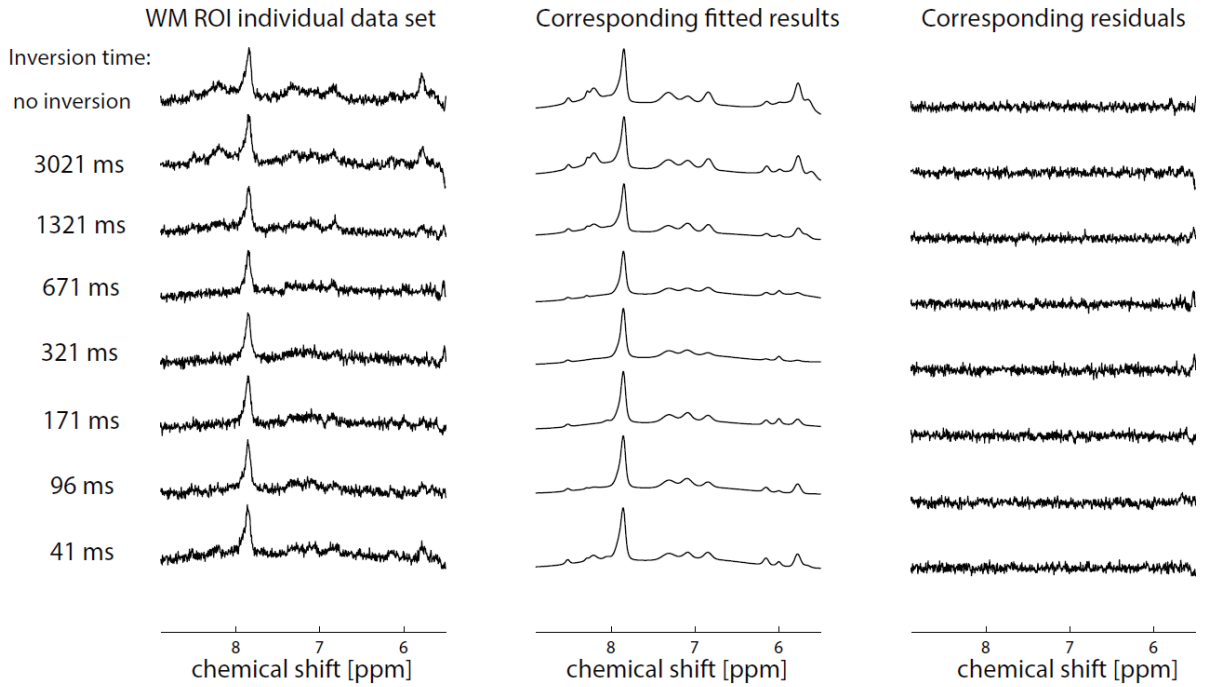

Supporting Figure S1: Representative WM ROI inversion transfer series from an individual volunteer, along with the corresponding fitted spectra and residuals, indicating the quality of the data for the WM ROI and the suitability of the model.

Final authors' version of "Fichtner et al. Magn Reson Med. epub 2017 Oct 16. doi: 10.1002/mrm.26968"

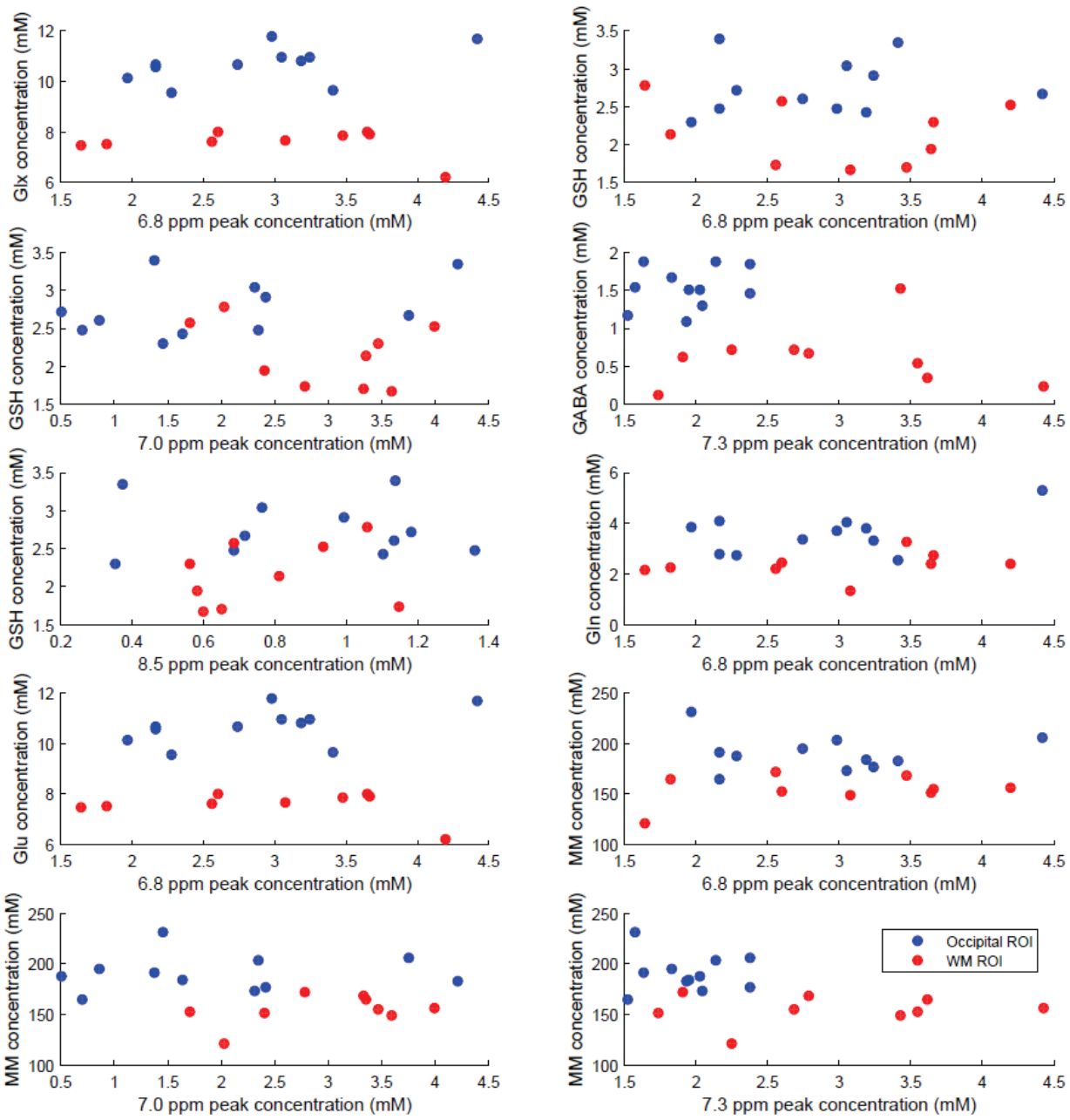

Supporting Figure S2: Scatter plots for the range of correlations tested between upfield and downfield peak areas. Occipital ROI data points shown in blue, WM ROI data points shown in red. The downfield peaks are along the x-axes, and the upfield peaks along the y-axes, as labeled in the figure.

Final authors' version of "Fichtner et al. Magn Reson Med. epub 2017 Oct 16. doi: 10.1002/mrm.26968"